Earth, Planets and Space

FULL PAPER Open Access

Characterized source model of the M7.3 2016 Kumamoto earthquake by the 3D reciprocity GFs inversion with special reference to the velocity pulse at KMMH16

Anatoly Petukhin[1*], Hiroshi Kawase[2], Fumiaki Nagashima[2] and Eri Ito[2]

Abstract

The 2016 Kumamoto earthquakes caused severe damage centering on the Mashiki residential area. The velocity waveforms at station KMMH16 in Mashiki, during the *M*7.3 mainshock, show large pulses. We found that severe damage in Mashiki may be the result of the strong westward velocity pulse. The question raised is how the near-fault ground motions with strong velocity pulse at KMMH16 were generated during the mainshock. We focus on the characterized source model with Strong Motion Generation Areas (SMGA). Empirical Green's function (EGF) method is widely used for source modeling in this case. However, in case that the target site is located just near the fault in nodal plane of source mechanism (like KMMH16), mechanism of the EGF event should perfectly fit mechanism of the mainshock, which is a rare case. Therefore, instead of using EGFs, we used theoretical 3D Green's functions. Our approach is a nonlinear source inversion. This method requires calculation of waveforms and comparison with observations for many source models. To accelerate these calculations, we use pre-calculated GFs by the reciprocity method in the JIVSM velocity structure model. By comparison with aftershock records, we validated this structure for periods as short as 1.5 s. Target sites are limited to sites close to the fault: KMM005, KMM006, KMMH14, and KMMH16. First, we look for an initial SMGA source model by the grid search method applied to relatively long-period (> 3 s) waveforms and coarse grid of source parameters. Then, we tune that source model to fit observed short-period waveforms with the simplex search method. Necessary physical constraints for the range of the source parameters are applied here. The important point in our inversion scheme is to describe the Kostrov-like slip velocity functions inside each SMGAs by using two triangles. The resulting source model agrees well with other inversion results. We found that the observed westward pulse at KMMH16 is the result of the constructive interference of two pulses from SMGA1 and SMGA2, located in Hinagu fault and southwestern segment of Futagawa fault.

Keywords 2016 Kumamoto earthquake, Source inversion, Reciprocity method, Strong-motion generation area, Characterized source model, Recipe for strong-motion prediction, Source time function

*Correspondence:
Anatoly Petukhin
anatolyp@geor.or.jp
Full list of author information is available at the end of the article

Graphical Abstract

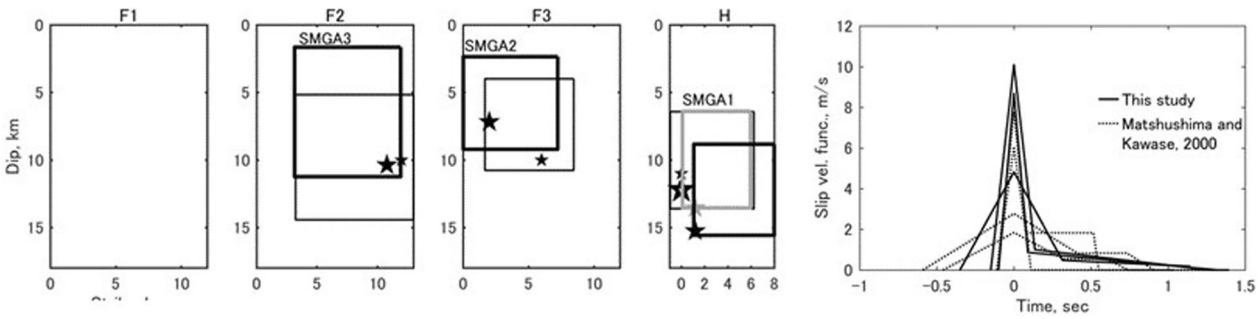

Introduction

The 2016 Kumamoto earthquakes caused severe damage centering on the Mashiki residential area (Fig. 1). For the *M*7.3 mainshock event (as well as the *M*6.5 foreshock event), extremely large ground motions with maximum peak ground accelerations greater than 1000 cm/s^2 were observed at one of the KiK-net stations, KMMH16, in the north of downtown Mashiki,

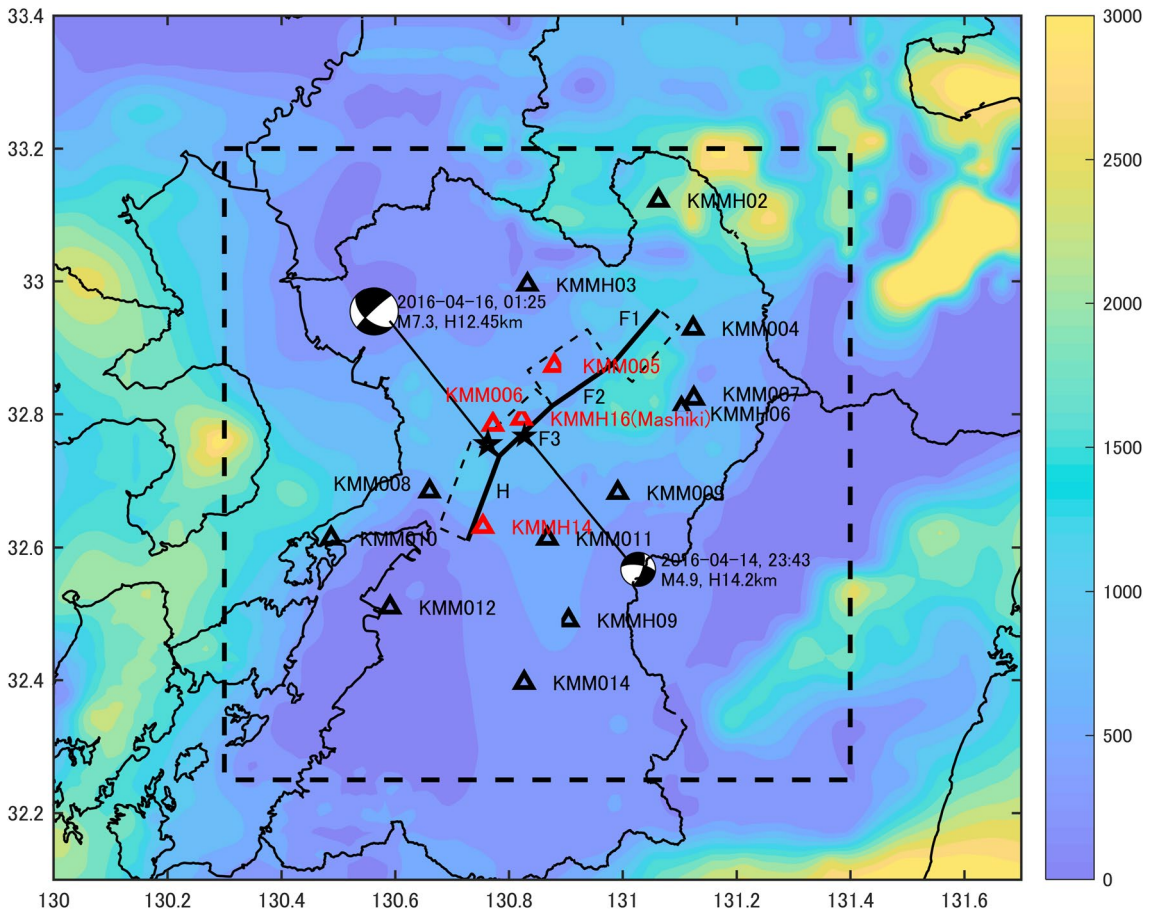

Fig. 1 Map of target area. Background is the depth of bottom interface of the *Vs* = 2 km/s layer of JIVSM model, in meters. Dashed square—target area of calculation, solid line—surface traces of the fault segments, triangles are K-NET and KiK-net sites within 50 km from fault (red—target sites for SMGA inversion, black—validation sites)

one of the closest stations to the causative fault (with the epicentral distance of about 7 km and just 2 km from the fault). The velocity waveforms at KMMH16 during the *M*7.3 event showed a large velocity pulses observed both by the surface and downhole (252 m below the surface) sensors.

It is understood that extremely high accelerations were remarkably amplified by soft layers near the surface (e.g., Kobayashi G. et al. 2017; Kurita 2017). From the viewpoint of the structural response, Kawase et al. (2017), found that severe damage in Mashiki may be the result of strong short-period (1 s) westward velocity pulse (see Fig. 2, pulse between 6-to-8 s in the EW component of the observed waveform). One of the important questions raised by the 2016 Kumamoto earthquakes but not resolved yet is how the near-source ground motions with strong velocity pulse at KMMH16 were generated during the *M*7.3 mainshock event.

For a site near the fault (like KMMH16), large velocity pulse in direction cross to the fault would be expected for a predominantly lateral rupture propagation on a strike-slip fault. Oppositely, pulse in the fault parallel direction is small. However, both additional normal component of slip and non-horizontal direction of rupture propagation can significantly change balance of pulses. See examples in Fig. 12 of Somei et al. (2019). In case of the *M*7.3 earthquake, right-lateral fault mechanism has significant normal component in the Futagawa segment (e.g., Asano and Iwata 2021), which can be confirmed by the general source mechanism of mainshock (by F-net): strike 226, dip 84, rake − 142 deg. To address the question of the velocity pulse generation, source models that can reliably explain observed ground motions (including short period pulses) in and around the source areas are necessary.

Most of the source waveform inversion results (Asano and Iwata 2016, 2021; Kubo et al. 2016; Yoshida et al. 2017; Kobayashi H. et al. 2017; Hallo and Gallovič, 2020) were able to explain a large eastward peak velocity (see Fig. 2, pulse between 8 and 11 s in the EW component of the observed waveform) and permanent displacement at the KMMH16. To reproduce them a LMGA (long-motion generation area, Irikura et al. 2020) at a shallow depth near KMMH16 site is required. However, a westward short-period peak velocity pulse before the large eastward pulse was underestimated in these simulations.

Inversion source models also indicate that there could be an upward rupture propagation toward KMMH16. With this finding at hand, Somei et al. (2019) used empirical Green's function (EGF) method (e.g., Irikura 1986) to demonstrate that the westward pulse at the KMMH16 can be a result of upward rupture propagation from the bottom of the fault toward the surface (e.g., Inoue and Miyatake 1997; Bouchon et al. 2002). However, without an additional large slip spot near KMMH16, the eastward pulse that created the crustal movement associated with the fault displacement is underestimated (see Fig. 9 of Somei et al. 2019).

The EGF method is widely used for forward source modeling because of its small number of parameters and is successfully reproducing broadband ground motions. However, in case that the target site is located just near the fault in the nodal plane of the source mechanism (like KMMH16), the mechanism of the EGF event (usually aftershocks) should perfectly fit the mechanism of

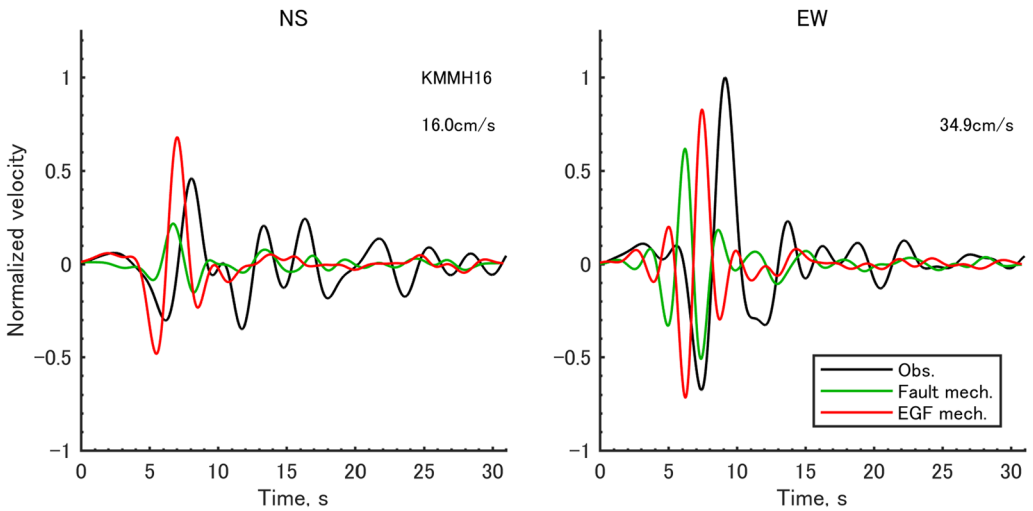

Fig. 2 Comparison of simulated (red and green) and observed (black) waveforms for SMGA model of Somei et al. (2019), for two cases of GFs: Case 1 (green line; source mechanism of GFs adjusted to the main fault) and Case 2 (red line; source mechanism of GFs adjusted to the EGF). Waveforms are normalized to the peak amplitude of observed waveform

the mainshock, which is a rare case. Otherwise, large variations of amplitudes in the vicinity of the nodal plane could produce large errors of ground motion synthetics.

Therefore, instead of using EGFs, we use theoretical Green's functions (GF) from the three-dimensional basin structure in the target area, combined with a nonlinear source inversion scheme. Our approach is a combination of the global optimization (grid search, GS) and the local search (simplex search, SS). This method requires calculation of waveforms and comparison with observations for many source models. To accelerate these calculations, we use pre-calculated GFs by the reciprocity method (Eisner and Clayton 2001; Graves and Wald 2001). For source parameter settings and comparison of results, we use source models of Somei et al. (2019) and Yoshida et al. (2017) as a reference for this study.

The issue of inconsistency of source mechanisms between the EGF event and the target earthquake, in case of the *M*7.3 Kumamoto earthquake, is clearly illustrated using the results of the Somei et al. (2019) study. For the source model of Somei et al. (2019), we initially compare 2 cases based on their source representation because we need to know why they successfully reproduced the westward pulse at KMMH16. Case 1 uses the source parameters of Somei et al. (2019) for three strong moion generation areas (SMGA), and 3D GFs (see paragraph "Calculation of reciprocal GFs and waveforms" below). GFs for each point subsource are calculated using the rise time $Tr = 0.37$ s, which is from velocity pulse width of observed waveforms at the nearest rock site to the EGF1 event from (Somei et al. 2019; M4.9 aftershock on April 14, 2016), but with the strike and dip angles adjusted to those of the plane segments of the 2016 Kumamoto earthquake. In Case 2 the strike and dip angles are taken from the EGF1 and EGF2 source mechanisms of Somei et al. (2019) so that the element sources are not aligned on the mainshock fault surface. The latter corresponds to the EGF calculation. Waveforms are bandpass filtered in 2-10 s. Comparison with the observed waveforms at KMMH16 is shown in Fig. 2. The synthetic waveforms for Case 1 are largely underestimated and shifted, while the synthetic waveforms for Case 2 have better fit. Especially, the high-amplitude westward pulse before the major eastward pulse is well-reproduced only in Case 2. We suppose that this discrepancy of the source mechanisms between EGFs used and the main fault, as mentioned above, should be the reason of the waveforms difference. We should notice that smaller time shift exists also in Case 2. However, similar time shift exists in waveforms in (Somei et al. 2019, Fig. 9), and this is not issue of the mechanism discrepancy. For the strong-motion prediction problem, timing of velocity peaks is not so important problem in comparison with the peak amplitudes. However, for understanding of the source features, e.g., SMGA depth and/or rupture initiation, shift of peak is critical. Correction of the shift is an additional motivation for this work.

In this study, similar to Irikura et al. (2017) and Somei et al. (2019), we focus on the characterized SMGA source models in which we are assuming several rectangular patches on the fault surface with the same slip velocity function in each patch. This kind of source model is adopted in Recipe for strong-motion prediction (Irikura and Miyake 2011). In the following sections, we first validate the velocity structure model at the target sites by waveform comparison for small earthquake. Then, S-wave arrival corrections by the evaluation of time shift between observed and simulated waveforms will be estimated. For estimation of the SMGA model parameters, i.e., locations, rupture initiation points, rupture propagation velocity, source time functions (STF), and so on, we will use combination of the GS and SS methods.

STF is an important parameter that requires special attention in the source modeling. From the physics-based dynamic rupture simulations (e.g., Tinti et al. 2005 and references therein; for recent studies see e.g., Pitarka et al. 2021, and references therein), we know that it should be the so-called Kostrov type with an initial sharp peak with a short duration together with a subsequent slow and steady slip. Matsushima and Kawase (2000) demonstrate that the model with Kostrov-like STF reproduces well destructive velocity pulses (killer-pulses) in the near-fault region during the 1995 Kobe earthquake. However, due to small number of time windows and inaccuracy of velocity structure models used for GF calculation, most of the kinematic source inversions with multiple windows, including examples above, do not reproduce Kostrov-like STFs. Constraining of STF to the Kostrov type is necessary and so Kostrov-type STF with two unknown parameters is assumed for inversion in this work.

Fault geometry, data, and velocity model

The 2016 Kumamoto earthquakes ruptured the Futagawa–Hinagu fault system. Source model consists of 4-plane segments related to these faults. Similar to Somei et al. (2019), we use the same 4-plane model (F1, F2, F3 and H) used for the source inversion by Yoshida et al. (2017, Table 1) with different dip angles as shown in Fig. 1. Depth of the top edge of model is 2 km. Subfault mesh size is assumed to be 400 m. and the number of subfaults is 6160.

For source inversion we choose 4 target sites nearest to the Futagawa–Hinagu fault: KMM005, KMM006, KMMH14 and KMMH16, shown in red triangles in Fig. 1. Although the observed structural damage in Mashiki was caused by ground motions on the surface,

the surface record at KMMH16 has nonlinear effects in the surface soil layers, recognized by a 0.5 s time delay of short period waveform (e.g., Sleep and Nakata 2019). For this reason, we use the downhole record at KMMH16 (depth 255 m, rotation angle 0 deg), whereas records on the ground surface are used for the other KiK-net sites. Off-fault KiK-net and K-NET sites shown in black triangles in Fig. 1 will be later used for validation of the resulting SMGA model.

The velocity model used is the three-dimensional Japan Integrated Velocity Structure Model (JIVSM, Koketsu et al. 2012), the 2015 release. It consists of 23 velocity layers and ready to use for numerical simulations of ground motions. JIVSM was carefully tested and compared with the J-SHIS model in the Kumamoto 2016 earthquake area. By comparing observed and simulated spectral amplifications it was found that JIVSM better reproduce observed data (The Headquarters for Earthquake Research Promotion 2019). The calculation area is in between 130.3 degree and 131.4 degree East, and 32.25 degree and 33.2 degree North, which is approximately ± 50 km from the fault. The depth of the model is 40 km and well below Moho interface. Reflections from Moho interface may reduce the effect of possible reflections from the bottom of the calculation volume (reflections despite of the absorbing boundary at the bottom). In the topmost layer of the JIVSM, *Vs* is 350 m/s. However, depth of this layer in the calculation area is negligibly small (64 m maximum). To accelerate simulations by the finite-difference method (FDM) we filled this layer by the second layer having *Vs* = 500 m/s. An example of the depth contour of the bottom interface of the layer with *Vs* = 2.0 km/s in the target area is also shown in Fig. 1.

We estimated the valid period range of the JIVSM model at the target sites. The event used as EGF1 in Somei et al. (2019), is used for validation. Waveforms are simulated using the F-net moment and source mechanism (*Mo* = 2.71e + 16 Nm, *strike* = 279, *dip* = 67, *rake* = − 22) and the JMA hypocenter location (32.767 N, 130.8273E, 14.2 km) and origin time (14 Apr 2016, 23:43:41.17). Rise time is *Tr* = 0.37 s, which is from velocity pulse width of observed waveforms at the nearest rock site. Other calculation parameters are: (1) waveform duration is 20 s; (2) minimum period *Tmin* is 1.0 s; (3) time step is 0.003 s; (4) FDM grid size is 100 m, which is equivalent to 5 grids per shortest wavelength; (5) here and below waveforms are filtered with the two-way 6th order Butterworth filter. Waveforms for three cases are compared: *Tmin* = 1.0, 1.5 and 2.0 s. A case with *Tmin* = 1.0 s resulted in the overestimation of amplitudes. Waveforms for *Tmin* = 1.5 and 2.0 have a good fit, i.e., the pulses shape and time delay agree with observed pulses and peak amplitude difference is within ± 2 times. It is assumed that *Tmin* = 1.5 s is the valid minimum period for all target sites. Results of the comparison with observed waveforms in case *Tmin* = 1.5 s are shown in Fig. 3. It is possible that some residual misfit of waveforms in Fig. 3 (i.e., larger amplitudes in EW component at KMM005 and KMM006, and smaller amplitudes in NS component at KMMH16) is result of inaccuracy of assumed source mechanism, while the overestimation for *Tmin* = 1.0 s is result of inaccuracy of the assumed *Tr* value. For correct validation of velocity structure by the waveform comparison, in ongoing work, Petukhin and Iwasaki (2021) proposed tuning of source parameters using the target velocity structure model (see also Asano et al. 2016).

The JIVSM velocity model has a complex 3D structure in the shallower layers. However, in contrast to the tomography results for the upper crust that have ± 10% velocity perturbations (e.g., Aoyagi et al. 2020), the assumed velocity inside the upper crust layer in the JIVSM model is uniform. For this regional scale variation and the homogeneity of shallow surface layers above the topmost *Vs* = 500 m/s layer of the velocity model, source inversion requires travel time correction for GFs. Regular practice is to align P-arrivals of observed and simulated waveforms that can be done automatically. Here, we calculated site-specific travel time corrections for S-waves as the difference between observed and simulated S-arrivals for aftershocks in the vicinity of SMGAs of Somei et al. (2019). Results are listed in Table 1. For details see Table 5 in Appendix.

Characterized SMGA source model

Similarly to Somei et al. (2019), we consider a 3-SMGA model with SMGA1, SMGA2 and SMGA3 within the fault segments H, F3 and F2, respectively. SMGAs are numbered in the sequential order of rupturing. Effect of the background area other than these SMGAs for high-frequency generation can be neglected (e.g., see explanation of the SMGA modeling in Miyake et al. 2003, and in Irikura et al. 2017 for the case of 2016 Kumamoto earthquakes). Each SMGA has its own rupture initiation point (that is, we assume a multi-hypocenter model). Distributions of the seismic moment density (i.e., final slip), the rupture velocity, and the source time function (STF) parameters are assumed to be uniform within each SMGA.

Results of the dynamic simulations demonstrate that the Kostrov-like STF is required for the physics-based ground motion simulations (e.g., Nakamura and Miyatake 2000; Tinti et al. 2005; Bizzarri 2012, and references therein). We will use simplest version of the Kostrov-type STF proposed by Graves and Pitarka (2004) and Guatteri et al. (2004). This STF consists of two triangles,

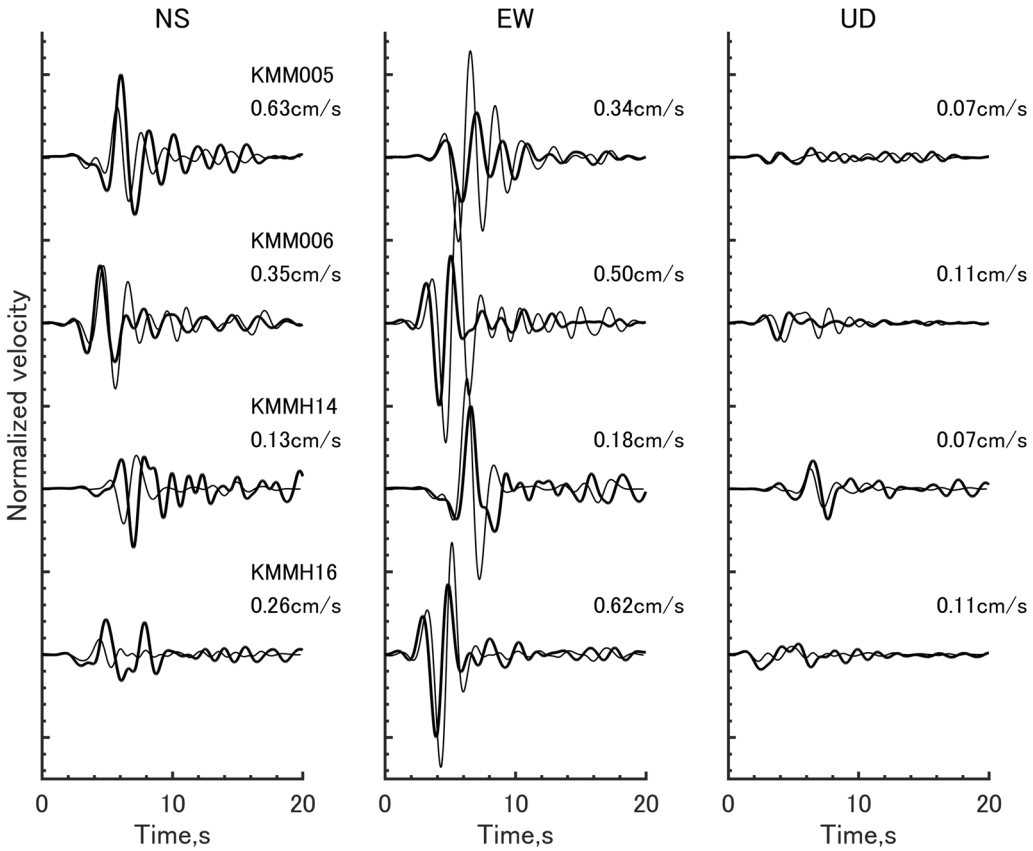

Fig. 3 Velocity structure validation. Comparison of observed (thick) and simulated (thin) velocity waveforms for Mw4.9 earthquake on 14 Apr 2016, 23:43 (EGF1 event in Somei et al. 2019), filter 1.5–10 s

short and long, and described by three parameters (see Fig. 4): the peak delay time *Tp*, the rise time *Tr*, and the amplitude ratio of a long triangle *Hr*. The short triangle is isosceles, and the corner of two triangles is adjusted to the descending slope of the short triangle accordingly with the assumed *Hr* value (i.e., the starting time of the long triangle equals to *Tp*(2-*Hr*) as shown in Fig. 4). Peak amplitude *Ap* is calculated from constraint:

$$\int_0^{Tr} STF(t)dt = 1.0. \quad (1)$$

Calculation of reciprocal GFs and waveforms

Our source inversion scheme requires forward simulations for hundreds-to-thousands source (SMGAs) models. In order to accelerate this process, we use pre-calculated GFs by the reciprocity method adopted to FDM simulations (Graves and Wald 2001; see also Matsushima and Kawase 2009; Petukhin et al. 2016). For an example of waveform fit between the forward and reciprocal waveforms, see Fig. 3 of Petukhin et al. (2016).

Table 1 Estimated *S*-wave travel time corrections for each site

Site	Target SMGA	*tS*-correction, s
KMM005	SMGA3	− 0.30 ± 0.05
KMM006	SMGA2	− 0.41 ± 0.07
KMMH14	SMGA1	− 0.23 ± 0.13
KMMH16	SMGA2	− 0.43 ± 0.05

At 1st step, reciprocity method calculates responses of the 3 point-forces applied at the target site location, in the X, Y and Z directions, i.e., three runs of the 3D-FDM for each target site. Resulted waveforms at each grid pair of the FDM double-couple source (see Graves 1996), are combined. Then the 2nd step is to make a source moment tensor response at the site. For more details see (Graves and Wald 2001). Therefore, we need 12 runs for four target sites in total. One run for the GF with duration of 20 s, requires 5 h calculation on our 32 CPU cluster. For a regular FDM method it would require 6,160 runs accordingly with the number of source grids, which is practically impossible. Other calculation parameters are: (1) GF

duration is set to be 20 s; (2) minimum period is 1.5 s; (3) FDM grid size is 150 m, which is equivalent to 5 grids per shortest wavelength; (4) time step is 0.0044 s. We should notice that costly 1st step that requires cluster computer for a few days, can be done in advance and results can be stored into memory. Calculations in the 2nd step that require source mechanism assumption, are fast and GFs for thousands of subsources can be calculated in a few hours on desktop computer.

To be able to calculate waveforms for a large variety of STF settings, namely *Tp*, *Tr* and *Hr*, we applied multi-window approach to express STF with arbitrary shape (Hartzell and Heaton 1983). See triangular windows shown by thin gray lines in Fig. 4. This approach greatly reduces time for waveform calculation because waveforms are synthesized simply by fast operations of GFs scaling and shift. GFs are calculated for triangular window, in which a rise time of 0.1 s was chosen to be short enough to reproduce correctly complicated forms of the Kostrov-like STF including short peaks.

We would like to calculate the basin responses to such STFs with a very sharp initial rise because what we are observing on the surface of the earth is the result of the convolution of the STF with the rupture propagation within each SMGA and therefore such a short initial pulse will contribute the sharpness of the observed pulse indirectly, and even after the filtering with $Tmin = 1.5$ s they are required by inversion, and therefore STFs with a sharp rise are physically resolvable.

Waveforms synthesized by the multi-window approach with a 0.1 s window are verified by comparison with regular FDM waveforms for the same STFs. For a longer waveform, another approach that requires spectral convolution of GFs to a target STF (Petukhin et al. 2017) may be necessary.

Two sets of GFs for $rake = 90$ deg and $rake = 180$ deg necessary to represent an arbitrary rake angle in the inversion are calculated effectively by the reciprocity method on a desktop computer after finishing FDM step and does not require additional set of costly FDM simulations on the cluster computer.

Inversion procedure

For the source inversion, the grid search (GS) allows a homogeneous exploration of the whole parameter space. However, it is computationally expensive. For example, in case of a search for 12 parameters (see Table 2) and a rough grid of only five points for each parameter, it will require one month for calculations for 244 million times of GS. To make this method effective, we combined it with a fine search by the simplex method (SS) after the GS and repeated the process iteratively.

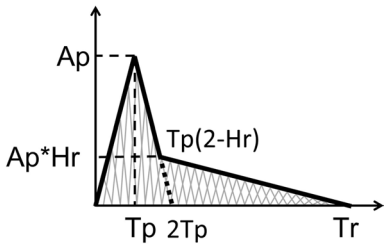

Fig. 4 A Kostrov-type triangular STF (after Graves and Pitarka 2004) used in this study

SS is derivative-free method developed by Lagarias et al (1998), and allows a stable search of the minimum value of the target function. It is implemented in Matlab and is ready to use. This method requires an initial model and searches the minimum value in the vicinity of the initial model. In preliminary inversions by the SS method and the initial model by Somei et al. (2019), we selected nine effective parameters for inversion: *Vra*, *Vrb*, *Rake*, *Tp*, *Mo*, *Lcent*, *Hcent*, *Lhypo*, *Hhypo*, and fixed other three parameters: *Sa*, *Tr*, and *Hr*, as shown in Table 2. This hybrid approach reduces the number of parameters for the GS and reduces its computation time to a reasonable value. Fixed parameters are:

1. SMGA area *Sa*: The SMGA size and rupture velocity *Vr* determine the waveform pulse width, however there is trade-off between them, as shown in e.g., Matsushima and Kawase (2000). We use SMGAs with the same size as in Somei et al. (2019).
2. Rise time *Tr*: This parameter is responsible for relatively long-period content of simulated waveforms, while their short-period peaks which are target of this study are defined primarily by *Tp*. For this reason, we fixed the rise time as half of rupture time across SMGA, $Tr = 0.5Wa/Vra$, where *Wa* and *Vra* is the width and *Vr* of each SMGA.
3. Amplitude of long triangle of the STF is fixed as a reasonable value $Hr = 0.1$, typical for dynamic STFs in the large slip-rate areas (which are SMGA equivalent, e.g., Yoshida et al. 2011). Although larger values are possible too, in preliminary simulations we did not notice effect of this parameter change.

To get the best-fit source model, we will use the GS and SS methods iteratively. In the 1st step, we will run GS for the set of effective parameters. In the 2nd step, we will make fine-tuning of the best model from the 1st step. By this two-step approach, we are going to look for a model that: (1) fit waveforms and is (2) physically reasonable (according to criteria assumed in Table 2).

Table 2 List of search parameters in this study. Value ranges are used in inversion

Name	Parameter description	Value
Vra	Rupture velocity in SMGA	2.0–3.0 km/s
Vrb	Background rupture velocity (velocity between adjacent rupture initiation points)	1.0–3.0 km/s
Rake	Rake angle. Strike and dip angles are defined by the fault segment	centered to − 180 deg
Tr	Rise time	fixed to half of rupture time across SMGA
Tp	Peak delay time, see Fig. 4	0.3–2.0 s
Hr	Relative amplitude of long triangle, see Fig. 4	fixed to 0.1
lg*Mo*	Decimal logarithm of seismic moment, Nm	17.5–18.5
Sa	SMGA area	fixed to Somei et al. 2019
Lcent	Center of SMGA in strike direction (from reference point of segment)	3.6–8.4 km
Hcent	Center of SMGA in dip direction (from reference point of segment)	3.6–14.3 km
Lhypo	SMGA hypocenter location in strike direction (from reference point of segment)	0.9–9.3 km
Hhypo	SMGA hypocenter location in dip direction (from reference point of segment)	2.9–17.0 km
tHypo	SMGA hypocenter time	Calculated as *Rhypo/Vrb*

Effectiveness of the SS method depends on the selection of an initial model. Namely, if an initial model is in the vicinity of the global misfit minimum, the search of the global minimum will be successful. If an initial model is in a different valley next to the valley of the global minimum, the result of search will be the minimum misfit model in that valley, not the one with the global minimum. Valleys of the waveform misfit function are defined by the fit (residual) of positive and negative motions of waveforms. It is easier to get a good initial fit of waves for long-period waveforms, than for short-period waveforms.

Waveform misfit *WM* adopted in the search is:

$$WM = \frac{\int_0^{t_D} (Vsim(t) - Vobs(t))^2 dt}{\sqrt{\int_0^{t_D} Vsim(t)^2 dt \cdot \int_0^{t_D} Vobs(t)^2 dt}}, \quad (2)$$

where $Vobs(t)$ and $Vsim(t)$ are observed and simulated waveforms, and t_D is the waveform duration, 20 s. For oscillating seismic waveforms, *WM* will have many minima and maxima depending on the waveforms shift. It is important to have an initial model in the vicinity of the global minimum of *WM* in the parameter space. Because the number of *WM* minima will increase as the minimum period *Tmin* of waveforms decreases, the probability that the initial model would be in the vicinity of the global minimum decreases. In order to guide the search process to the global minimum of the targeted short period (*Tmin* = 1.5 s in our case) in the end, we will use an approach in which the minimum period of waveforms used for SS gradually decrease from 4 s to 3, 2, and 1.5 s. This procedure allows us to keep the initial model on each step in the vicinity of the global minimum, and we apply it every time when we "perform SS".

It is important to keep the search results within the physically allowed ranges of parameters listed in Table 2. To do this we apply the penalty constraint, i.e., if a parameter is going outside of allowed range, some penalty value, added to the *WM* value, allow artificially increase misfit in this search direction. For example, from source inversion results (Miyakoshi and Petukhin 2005) and dynamic simulations, we know that $Vra > Vrb$. This condition requires constraining by penalty. Moreover, to allow the search process to cross ridges between the minima, this penalty should not be too strong. Finding a proper penalty value by trial-and-error is an important case-study step.

In order to reduce the number of parameters for GS step of inversion, we use an observation that the waveform at the near-fault site can be reproduced by the large slip area or SMGA nearest to that site (e.g., Kubo et al. 2016; Yoshida et al. 2017; Somei et al. 2019). Otherwise, GS for all three SMGAs simultaneously would have computation time increased 27 times, which is practically impossible. Therefore, we assume that KMMH14 can be used for initial SMGA1, KMMH16 for SMGA2, and KMM005 for SMGA3.

We applied next procedure for the characterized source inversion; see Fig. 5.

Step 1. Rough GS search for SMGA1 and KMMH14.

Step 2. Use result of Step 1 as initial model for the fine fit of SMGA1 by the SS method.

Step 3. Rough GS search for SMGA2 and KMMH16.

Step 4. Use result of Step 3 as initial model for the fine fit of SMGA2 by the SS method.

Step 5. Rough GS search for SMGA3 and KMM005.

Step 6. Use result of Step 5 as initial model for the fine fit of SMGA3 by the SS method.

Step 7. Combine SMGAs from Steps 2, 4, and 6.

Step 8. Use the result of Step 7 as the initial model for the fine fit of all SMGAs by the SS method. Target sites are KMM005, KMM006, KMMH14 and KMMH16.

At Steps 2, 4, 6 and 8, as mentioned above, gradual decreasing of minimum period is applied.

The SS stops when difference of the model parameters and of the misfit function between two successive iterations is below the tolerance value. Tolerance should be small enough in order to allow search process to move through valleys with gentle slope, but should not be too small to allow finish of search in a reasonable time. Adopted tolerance in SS is 0.01, which allow us to finish the search in several hundred iterations that require one night for calculations so that next morning we could see results of settings in the previous day, revise them and repeat again (tolerance is a lower bound on the change of variable or misfit in iteration).

For the full list of grid values and penalty constraints, see Tables 6 and 7 in the Appendix. Combination of SS method with a more regular GS method allows inversion with a reasonable computation cost. Getting of the SS resolution by GS method along would require too high computation cost.

The locations and rupture initiation points of SMGAs at Steps 1, 3, and 5 by GS and Steps 2, 4, and 6 by SS are shown in Fig. 6. Other SMGA parameters are listed in Table 3. Location of SMGAs roughly agree with other studies (e.g., Somei et al. 2019), even if we used only one site for inversion of each SMGA. This is an additional proof of validity of the one site approach. Locations of rupture initiation points for SMGAs indicate the existence of the upward rupture propagation and subsequent directivity effect toward the corresponding target sites. Values of *Tp* are small that indicate short-period (1.5 s or less) pulses generation in SMGAs. Both rupture velocities inside SMGAs and background (between SMGAs) have the sub-shear values.

In Fig. 7 we compare simulated and observed waveforms at the target three sites. Figure 7 also compares waveforms for the combined model at Step 7. Due to interference of waves from neighboring SMGAs, *WM* values degraded for NS component at KMM005, and EW components at KMMH14 and KMMH16. More problematic for this study is that westward pulse in question, marked by arrow in Fig. 7, also degraded at Step 7. To restore this pulse, at Step 8 we applied SS additionally for a model having all three SMGAs. This model includes interference effects between SMGAs. Results are described in the next section.

Inversion result, validation, and further tuning

Figure 8 shows the locations and rupture initiation points of SMGAs of the inverted model in Step 8. Other parameters are listed in Table 4. Figure 9 shows that simulated waveforms (marked as "Inv.") fit well observed waveform, including the destructive westward pulse at KMMH16 (Mashiki, see Kawase et al. 2017). Analysis of waveforms separately for each SMGA (marked as "S1", "S2", and "S3") indicates that this pulse may be the result of the constructive interference of waveforms from SMGA1 and SMGA2.

SMGA2 and SMGA3 in our inversion model reasonably agrees with models of Yoshida et al. (2017), and Somei et al. (2019). They are shallower than SMGAs of Somei et al. (2019), but better agree with the high moment-rate areas of Yoshida et al. (2017). This enhances upward directivity for SMGA3. For SMGA2 both the location and rupture initiation point are slightly shallower than those in Somei et al. (2019), and for this reason we expect a similar upward rupture directivity in general. On the other hand, the rupture initiation point for SMGA2 is shifted eastward from that of Somei et al. (2019), and so it allows a bit backward (westward) rupture propagation, which is physically possible in heterogeneous ruptures (e.g., Iwata and Sekiguchi 2002; Sekiguchi et al. 2006; Petukhin et al. 2022) but a rare case. We should notice that the rupture initiation point for SMGA2 is close to rupture initiation for SMGA3 and both are on the bend between the segments F2 and F3. Such fault bends cause stress concentrations and secondary rupture initiations become reasonable (e.g., Oglesby and Mai 2012). Parameters in Table 4 for SMGA2 and SMGA3 are also similar with model of Somei et al. (2019), and with parameters proposed by the Recipe (Irikura and Miyake 2011; The Headquarters for Earthquake Research Promotion 2017).

Although the location and rupture initiation point for SMGA1 also have similarity with results of Yoshida et al. (2017), and Somei et al. (2019), the moment value of SMGA (inversion value on the left in Table 4) is much larger than Somei et al.'s. To check if this value is reasonable or not, we tried to validate our results by the forward simulation and waveform comparisons for sites that were not used for inversion. Locations of 12 validation sites are shown as black triangles in Fig. 1, and for waveform comparisons see Fig. 10. Considering that our model is a simplified characterized SMGA model, adopted for the strong-motion prediction problem in the Recipe, waveform agreement is good, especially in the north and east of the fault. In the southwestern side of the fault, in direction of the SMGA1 location, waveform amplitudes are overestimated (sites KMM008, KMM010, KMM011, KMM012, KMM014, KMMH09).

In order to get better fit for the 12 validation sites and keep good fit for the target sites, we made manual tuning of the SMGA model. We called the resultant model as the "tuned model". The pre-calculated GFs allowed us

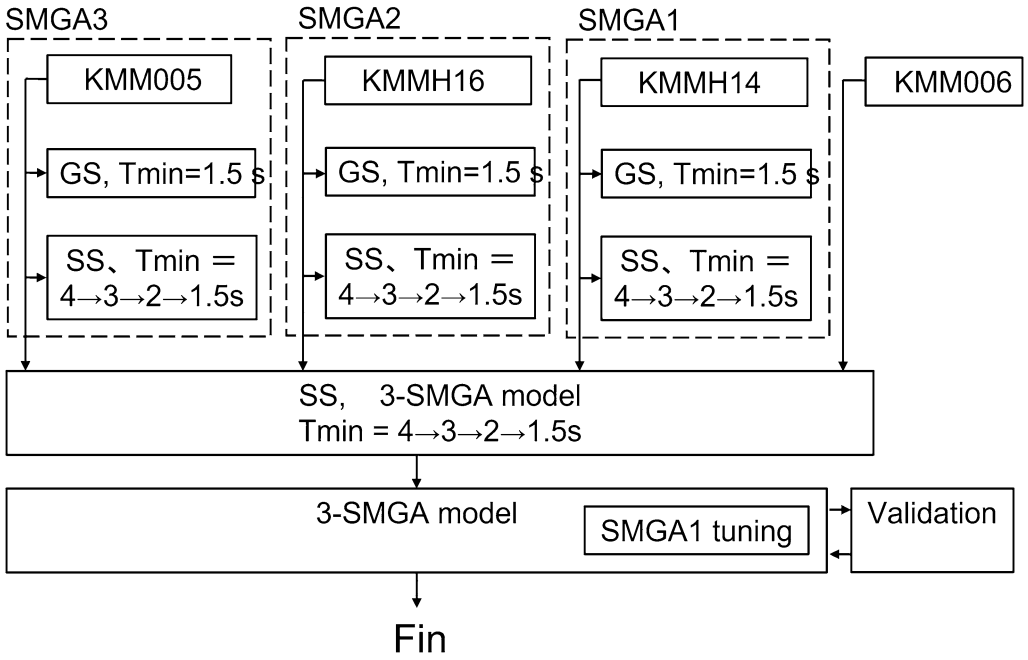

Fig. 5 Flowchart of the inversion method. GS—grid search, SS – simplex search

to make tuning in a real time: simulate waveforms in a minute, analyze result, change target parameter value, and calculate next waveform. The major rules for tuning are:

1. Decreasing of the *Mo* value for SMGA1 decreases amplitudes at the sites in the southwestern side.
2. Decreasing the depth of SMGA1 increases amplitude at the site closest to SMGA1 without increasing of amplitude at other distant sites.
3. Increasing of *Vrb* makes the arrival of wave pulses earlier.
4. Balancing of the arrival times of pulses from SMGA1 and SMGA2 regulates the width of the westward pulse at KMMH16. We found this approach more effective for tuning of the pulses width than tuning of *Vra* and *Sa*.

The location and parameters of the tuned model are shown in Fig. 8 (a gray rectangular) and Table 4. Comparison of waveforms for the target sites in Fig. 9 (the second and third waveforms for the inversion model and tuned model, respectively) demonstrates that the waveforms keep good fit to those observed ones at the

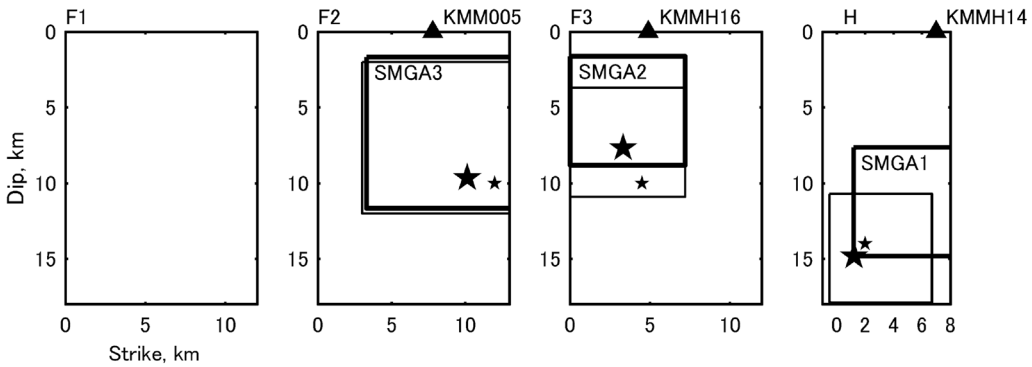

Fig. 6 Locations of SMGAs and rupture initiation points at Steps 1, 3 and 5 of the inversion procedure (GS, thin lines and small stars), and at Steps 2, 4 and 6 (SS, thick lines and large stars)

Table 3 SMGA parameters at Steps 1 to 6 of the inversion procedure (by grid search, GS, and simplex search, SS). For location of SMGAs and hypocenters, see Fig. 6

	SMGA1, KMMH14		SMGA2, KMMH16		SMGA3, KMM005	
	GS	SS	GS	SS	GS	SS
Mo, Nm	5.6e18	3.26e18	5.6e18	2.08e18	11.0e18	5.51e18
Slip, m	3.46	2.02	3.46	1.29	3.52	1.77
Vr, km/s	2.40	2.52	2.40	1.80	2.90	2.69
t0, s*/*Vrb*, km/s	1.87/2.00	1.53/2.45	5.35/1.50	4.18/2.04	5.73/2.30	5.50/2.40
Tp, s	0.50	0.17	1.00	0.12	2.00	0.35
Tr, s**	1.50	1.43	1.50	2.00	1.72	1.86
Ap, m/s***	6.59	7.94	3.55	5.17	1.87	4.34
Rake	− 180	− 176	− 135	− 144	− 195	− 201

* Rupture initiation time *Vrb* is calculated in the inversionand translated into t0. ** Rise time *Tr* in this study is calculated as a half oftravel time across SMGA. *** Peak slip velocity *Ap* is calculated from *Tp*, *Tr* andSlip values.

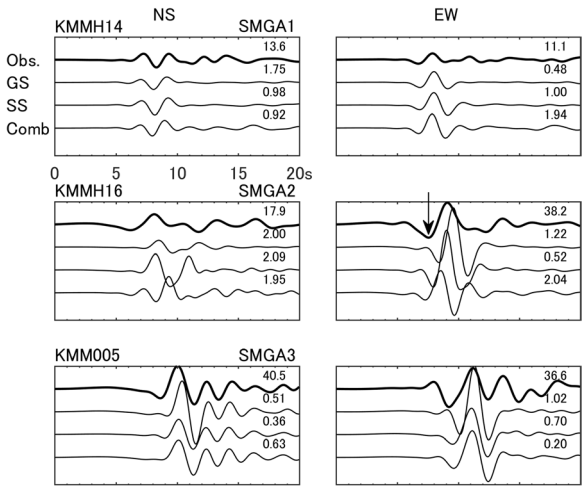

Fig. 7 Comparison of the observed (thick) and synthetic (thin) velocity waveforms at the target sites for the models in Table 3 and Fig. 6, with the period range of 1.5–10 s. GS grid search waveforms at Steps 1, 3 and 5; SS grid search waveforms at Steps 2, 4 and 6; Comb waveforms for the combined model at Step 7. Peak velocities are shown for the observed waveforms, whereas misfit *WM* are shown for the synthetic waveforms (the scales of amplitudes are common for all plots). Arrow indicates the westward pulse at KMMH16

target sites, except for the NS component at KMMH14, which is the site under the direct influence of SMGA1.

Discussion

The total moment M_0 of SMGA model in this study is 1.09e19 Nm. It agrees well with the total moment of the EGF model of Somei et al. (2019), 0.97e19 Nm, but significantly smaller than the total moment of the waveform source inversions: 4.7e19 Nm by Yoshida et al. (2017), 4.89e19 Nm by Asano and Iwata (2021), 5.6–7.3e19 by Hallo and Gallovič (2020), and 4.42e19 by F-net (the NIED CMT solution). The fact that short period ground motions are well reproduced by the SMGA models with 4–5 times smaller M_0, confirm that short period strong-motion generation in background area outside of SMGAs is not so important (Miyake et al. 2003).

One reason of the small short period strong-motion generation in background area outside of SMGAs is in the STFs of background area. For example, Pitarka et al. (2021) by their dynamic source modeling validated for 2019 Ridgecrest earthquake, demonstrate that STFs in background area have larger rise time and smaller Kostrov's peak. Schmedes et al. (2010) made bulk analysis of dynamic ruptures (non-validated) and found that *Tp* is short in areas of large peak slip velocity (i.e., SMGA) and become longer in areas of small peak slip velocity (i.e., background area). This reduces short-period content of the generated waves. Another possible reason is chaotic multi-front rupture propagation in background area in case of heterogeneous rupture (e.g., Petukhin et al. 2022), as well as already mentioned effect of smaller rupture velocity in background area. Both effects of rupture propagation reduce generation of short-period directivity pulses. Finally, comparison of simulated waveforms for source inversion results with and without background area (Ikeda et al. 2002; Sekiguchi et al. 2006; Wu et al. 2008; Yoshida et al. 2011; Poiata et al. 2012) also demonstrates that waveform peaks can be well reproduced solely by asperities without background area.

In Table 4, in addition to the comparison of our result with the EGF model of Somei et al. (2019), we compared source parameters with the Recipe values. Considering range of validity (about ± 1.5 times), the agreement is very good. The *Tp* of SMGA1, SMGA2 and SMGA3 are 0.15, 0.1 and 0.35, respectively. Recipe *Tp* value is estimated as $1/fmax$, where $fmax$ is the high-frequency cutoff (Hanks 1982). Current version of Recipe recommends $fmax = 6$ Hz for inland earthquakes (Tsurugi et al. 1997), which means

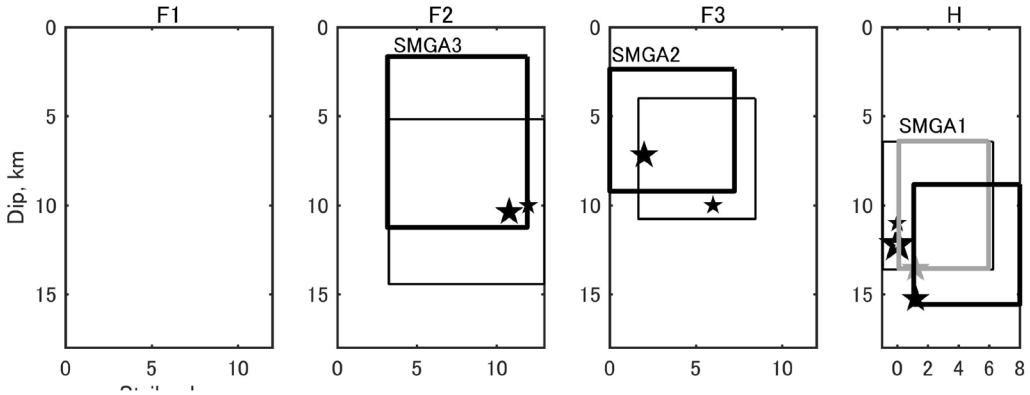

Fig. 8 The locations and rupture initiation points of SMGAs in this study (thick lines and large stars) compared with model of Somei et al. (2019) (thin lines and small stars). A rectangle in a black line and star indicate the location and rupture initiation point of SMGA1 from the inversion model, while that in a gray line and star indicate those from the tuned model

Table 4 SMGA parameters in this study and comparison with Somei et al. (2019), and Recipe. For location of SMGAs and hypocenters, see Fig. 8

		This study		EGF (Somei et al. 2019)	Recipe** (Irikura and Miyake 2011)
		Inversion model	Tuned model****		
SMGA1	*Mo*, Nm	6.42e18	3.16e18	2.08e18	3.22e18
	Slip, m	3.97	2.08	1.25	2.2
	Vr, km/s	2.52		2.8	2.4
	*t*0, s/*Vrb*, km/s	1.59/2.51	1.53/2.6	0.71/2.81	1.66/2.4
	Tp, s	0.15		–	0.17***
	Tr, s*	1.43		0.6	1.5
	Strike, dip, rake	205, 72, − 196		279, 67, − 22	-
SMGA2	*Mo*, Nm	2.26e18		2.08e18	3.22e18
	Slip, m	1.40		1.25	2.2
	Vr, km/s	2.53		2.8	2.4
	*t*0, s/*Vrb*, km/s	6.60/1.70		2.26/2.80	4.68/2.4
	Tp, s	0.10		–	0.17***
	Tr, s*	1.42		0.6	1.5
	Strike, dip, rake	226, 77, − 133		279, 67, -22	–
SMGA3	*Mo*, Nm	5.74e18		5.49e18	8.64e18
	Slip, m	2.00		1.72	3.2
	Vr, km/s	2.50		2.8	2.4
	*t*0, s/*Vrb*, km/s	5.89/2.42		3.50/3.79	5.94/2.4
	Tp, s	0.35		–	0.17***
	Tr, s*	2.00		0.6	2.08
	Strike, dip, rake	236, 65, − 174		230, 38, − 112	–

* Rise time in this study is calculated as a half of traveltime across SMGA. ** Assumed fault length is 38 km (i.e., without segmentF1). *** Calculated as $Tp = 1/fmax$, where $fmax = 6$ Hz (recommendedby Recipe). **** Parameters not menshioned for Tuned model are the same as for Inversion model

Tp is considered to be 0.167 s. Also, Tsurugi et al. (2020) found that for 2016 Kumamoto earthquake $fmax = 7.1$ Hz, which is slightly larger than the Recipe recommendation.

In Fig. 11, we compare STFs in this study with STFs of similar SMGA model for 1995 Kobe earthquake by Matsushima and Kawase (2000). Both earthquakes have similar magnitude and similar destructive velocity pulses, e.g., see Yoshida et al. (2005) in case of 1995 Kobe earthquake, and Kawase et al. (2017) in case of 2016 Kumamoto earthquakes. Figure 11 confirms that STFs for both earthquakes are also similar.

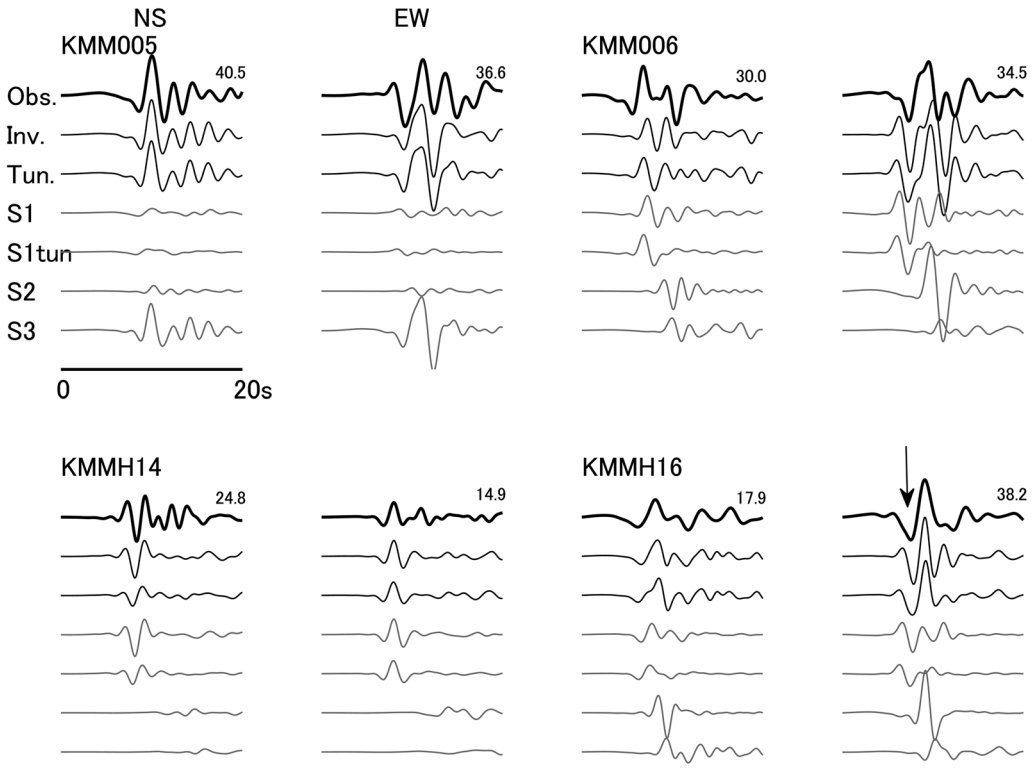

Fig. 9 Comparison of the observed (thick), synthetic (thin) and SMGA (gray) velocity waveforms at target sites for the models in Table 4 and Fig. 8, with a period range 1.5–10 s. The second waveform is for inverted model, and third waveform is for the moment-tuned model for SMGA1. Waveforms labeled "S1", "S2" and "S3" are, respectively, for SMGA1, SMGA2 and SMGA3 of inverted model. Waveforms labeled "S1tun" are for SMGA1 of tuned model. Arrow indicates the westward pulse at KMMH16

Conclusions

We estimated an SMGA source model for the *M*7.3 2016 Kumamoto earthquake (mainshock) by using a combined method of the grid search and the simplex search. In the SMGA model, we assumed that only SMGAs generate strong motions and contributions in the background fault rupture outside of SMGAs are neglected. Green's functions are calculated by the reciprocity method and the 3D JIVSM velocity structure model of The Headquarters for Earthquake Research Promotion (Koketsu et al. 2012). The target period range is from 1.5 to 10 s, and the target sites are KMM005, KMM006, KMMH14, and KMMH16, all close to the assumed fault plane. The initial 3-SMGA source model is estimated by the grid search method. Grid search applies separately to each SMGA, using record at the nearest site. Next, for fine-tuning of the initial model, we applied the simplex search method, again, separately to each SMGA, using the record at the nearest site. After combining the three obtained SMGAs, we applied again the simplex search method for three SMGAs using all four target sites at the same time. We called the resultant model the inversion model. Then, the inversion model was validated by comparing waveforms at 12 sites that were not used in the inversion. However, amplitudes at the sites close to the SMGA1 are overestimated. To improve the waveform fit at these validation sites, additional manual tuning was applied to SMGA1. In the resulting model, the locations of both SMGA2 and SMGA3 are shallower than those of the model in Somei et al. (2019), however, they have better correspondence with the higher moment-rate areas in Yoshida et al. (2017), as shown in their Fig. 9. The location of SMGA1 agrees well with both studies. The rupture initiation point of SMGA1 has a physically reasonable location near the mainshock hypocenter, while those of SMGA2 and SMGA3 have also physically plausible locations on the fault segment boundary (e.g., Oglesby and Mai 2012) very close to each other. As a result, we see primarily a backward (westward) propagation of rupture within SMGA2, opposite to the global rupture direction from the hypocenter.

We found that the synthetic waveform successfully reproduces a short-period westward pulse before the main eastward pulse in the EW component at KMMH16, as a result of the constructive interference of two pulses from SMGA1 and SMGA2. Our inverted source model here is a kind of an end-member of distinctive characteristics with a least number of unknowns based on the assumption established from

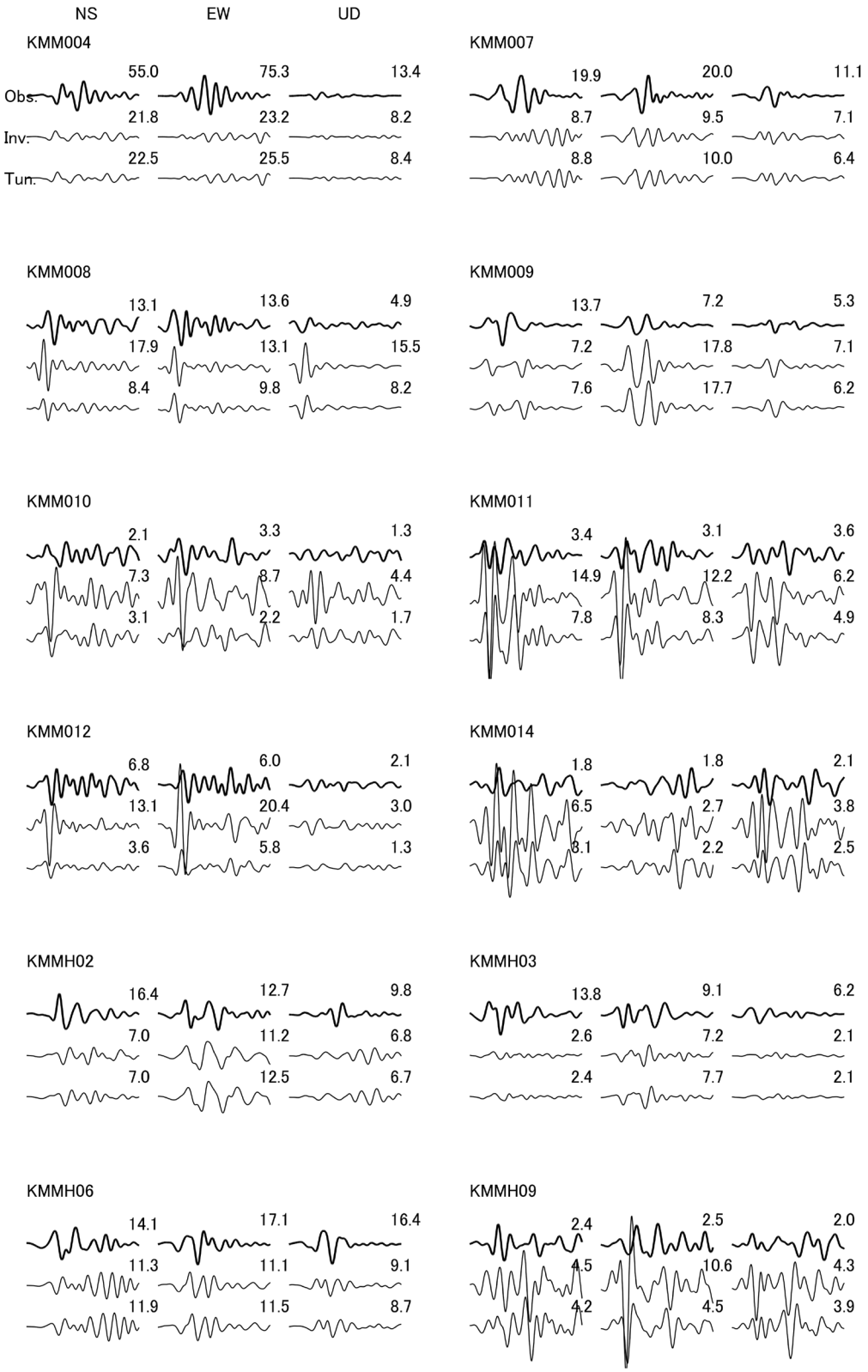

Fig. 10 Comparison of the observed velocities (thick) and the synthetic velocities (thin) for the 12 validation sites in Fig. 1, period range 2–10 s, waveform length is 30 s. The number in the right-hand side of each waveform is the peak amplitude in cm/s. For plotting, waveforms are scaled to the observed peak amplitude at each site

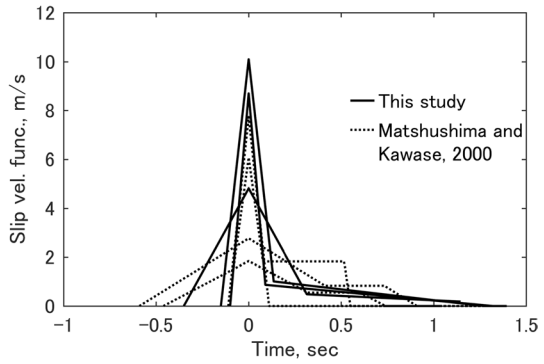

Fig. 11 Comparison of the slip velocity functions for 2016 Kumamoto earthquake (this study, solid lines) and for 1995 Kobe earthquake (Matsushima and Kawase 2000, dotted lines). All STFs are centered to their peaks. Wider STFs are for lager SMGAs in both studies

the empirical Green's function method (Irikura and Miyake 2011). Because of the limited amount of freedom of choices, the waveform fit is not as good as the conventional source inversions with a lot of elemental sources with their varying source time functions. However, thanks to the smaller degrees of freedoms in our scheme, we can delineate the detailed mechanism of the conspicuous westward velocity pulse at KMMH16 as mentioned above, where the clear concentration of the severe structural damage was observed (Kawase et al. 2017).

Appendix

See Tables 5, 6, 7.

Table 5 Parameters of records and t_S corrections

N	Site	Date	Time (JST)	Lat/Long/*H* [km]	*Mj*	t_{Sobs} [s]	t_{Sray_jma} [s]	*Hcorr* [km]	t_{Sfdm} [s]	Δt_S t_{Sfdm}-t_{Sobs} [s]
1	KMM005	4/16	8:8:50.62	32.855/130.851/11.1	3.9	2.69	3.49		3.72	
2	KMM005	4/16	17:17:49.39	32.856/130.861/10.7	3.5	2.73	3.32		3.51	
3	KMM005	4/17	0:3:33.48	32.861/130.851/14.1	3.4	4.20	4.26	− 0.2	4.51	− 0.32
4	KMM005	4/18	8:35:43.02	32.870/130.873/10.2	4.2	2.99	3.09	− 0.3	3.32	− 0.34
5	KMM005	4/16	22:53: 1.41	32.869/130.839/13.5	3.4	4.02	4.15	− 0.4	4.44	− 0.41
6	KMM005	4/17	0:45:48.51	32.875/130.887/11.0	3.1	3.17	3.32	− 0.5	3.55	− 0.38
7	KMM005	4/20	17:40: 8.49	32.863/130.841/12.5	3.0	3.89	3.89	− 0	4.16	− 0.27
8	KMM006	4/16	5:43:22.89	32.775/130.776/11.0	3.4	3.33	3.36	− 0.1	3.78	− 0.45
9	KMM006	4/16	10:26:10.42	32.803/130.847/11.2	3.8	2.94	3.90		4.36	
10	KMM006	4/19	12:52:14.02	32.776/130.779/10.8	4.0	3.27	3.30	− 0.1	3.73	− 0.46
11	KMM006	4/21	21:52: 3.39	32.785/130.832/11.0	4.0	3.80	3.66	+0.5	4.13	− 0.33
12	KMM006	4/16	3:27:30.74	32.802/130.819/11.8	3.2	2.99	3.73		4.14	
13	KMMH14	4/16	2:4:11.03	32.746/130.737/12.3	4.9	5.34 (5.44)	5.18	+0.5	5.56	− 0.22
14	KMMH14	4/16	16:2: 1.03	32.699/130.720/12.3	5.4	4.18 (4.19)	4.30	− 0.4	4.70	− 0.52
15	KMMH14	4/16	16:57: 6.92	32.695/130.723/11.3	3.2	4.01 (3.99)	3.99	+0.1	4.18	− 0.17
16	KMMH14	4/22	7:47:42.02	32.701/130.727/11.1	3.8	4.04 (4.02)	4.03	+0	4.26	− 0.22
17	KMMH14	4/16	22:25: 0.24	32.700/130.717/12.8	3.2	4.49 (4.49)	4.45	+0.1	4.67	− 0.17
18	KMMH14	4/17	16:8:51.09	32.707/130.728/10.3	3.6	4.03	3.97	+0.2	4.13	− 0.10
19	KMMH14	4/20	19:0:10.63	32.753/130.751/10.3	3.9	5.29 (5.14)	5.00		5.23	
20	KMMH14	4/24	18:50:15.97	32.695/130.719/11.5	3.6	4.03	4.06	− 0.1	4.26	− 0.22
21	KMMH16	4/16	4:5:49.20	32.797/130.813/12.3	4.0	2.50	3.59		4.00	–
22	KMMH16	4/16	10:26:10.42	32.803/130.847/11.2	3.8	2.01	3.37		3.73	
23	KMMH16	4/19	12:52:14.02	32.776/130.779/10.8	4.0	3.33(3.42)	3.43	− 0.3	3.82	− 0.49
24	KMMH16	4/21	21:52: 3.39	32.785/130.832/11.0	4.0	3.27(3.27)	3.26	+0	3.66	− 0.39
25	KMMH16	4/16	3:46:37.88	32.806/130.828/10.1	2.5	1.92	2.99		3.34	
26	KMMH16	4/16	5:43:22.89	32.775/130.776/11.0	3.4	3.50	3.52	− 0.1	3.92	− 0.42

t_{Sobs} hypocentral S-wave arrival time from observed records; in brackets are S-wave arrival time from the JMA arrival time list when available. Notice a good fit between t_S from JMA list and picks from records in this study. t_{Sray_jma} arrival time calculated by ray tracing and JMA velocity model. It is assumed that disagreement between t_{Sobs} and t_{Sray_jma} values is due to inaccuracy of the hypocenter depth estimation. *Hcorr* proposed depth correction. t_{Sfdm} S-wave arrival time from synthetic waveforms calculated with the JIVSM model. Δt_S S-wave site correction. For estimation of the average site corrections, we excluded records having large *Hcorr* > 0.5 km (struck-out values).

Table 6 Set of the grid parameter values for the GS search

Parameter	*Number of grids*	*Grid values*
Tp(s)	3	{0.5, 1.0, 2.0}
Vra(km/s)	4	{2.0, 2.4, 2.7, 2.9}
Vrb(km/s)	5	{1.5, 1.75, 2.0, 2.3, 2.6}
Rake(deg)	6	{— 120, — 135, — 150, — 165, — 180, -195}
Lcent(km)	4	{3.6, 5.1, 6.6, 8.4}
Hcent(km)	6	{3.6, 5.3, 7.3, 9.3, 11.3, 14.3}
Lhypo(km)	4	{4.5, 6.0, 7.5, 9.3}
Hhypo(km)	3	{10.0, 14.0, 18.0}
lg*Mo*(Nm)	3	{18.15, 18.30, 18.45}

Table 7 Set of the penalty constraints for the SS search

Param	Penalties for the WM value
Tp	$-1.0 \times \sum_{i=1}^{3} \ln(Tp(i)/0.5)$
Vra	$+3.0 \times \sum_{i=1}^{3} \lvert\ln(Vra(i)/2.52)\rvert$
Vrb	$+1.0 \times \sum_{i=1}^{3} \lvert\ln(Vrb(i)/2.52)\rvert$
Lcent	$+10 \times \sum_{i-1}^{3} \left(Lcent(i)\left\langle \frac{La(i)}{2} \cup Lcent(i)\right\rangle L_0(i) - \frac{La(i)}{2}\right)$
Hcent	$+10 \times \sum_{i=1}^{3} \left(Hcert(i)\left\langle \frac{Ha(i)}{2} \cup Hcert(i)\right\rangle H_0(i) - \frac{Ha(i)}{2}\right)$
Lhypo	$+10 \times \sum_{i=1}^{3} \left(Lhypo(i)\left\langle \frac{Lcent(i)}{2} \cup Lhypo(i)\right\rangle H_0(i) - \frac{Lcent(i)}{2}\right)$
Hhypo	$+10 \times \sum_{i=1}^{3} \left(Hhypo(i)\left\langle \frac{Hhypo(i)}{2} \cup Hhypo(i)\right\rangle H_0(i) - \frac{Hhypo(i)}{2}\right)$
lg*Mo*	$+1.0 \times \sum_{i=1}^{3} \lvert\lg Mo(i) - \lg Mo0(i)\rvert$

*Here: $L_0 = \{8, 12, 12\}$, $H_0 = \{18, 18, 18\}$, $La = \{7.2, 7.2, 10\}$, $Ha = \{7.2, 7.2, 10\}$, lg*Mo*0 is the GS result

Abbreviations

GF	Green's function
3D	Three dimensional
EGF	Empirical Green's function
SMGA	Strong-motion generation area
JIVSM	Japan Integrated Velocity Structure Model
GS	Grid search
SS	Simplex search
J-SHIS	Japan Seismic Hazard Information Station
FDM	Finite-difference method
STF	Source time function
NS	North–south
EW	East–west
CMT	Central moment tensor

Acknowledgements
Strong motion data from K-NET, KiK-net, and CMT solutions from F-net, are provided by the NIED. Hypocenter catalogs are provided by JMA. We are thankful to K. Somei and K. Yoshida for providing their source models and for fruitful discussions. To calculate Recipe source mode, we used scripts provided by M. Tsurugi. We are also thankful to two anonymous reviewers for helpful comments that strongly improved manuscript.

Author contributions
AP and FN performed simulations and inversion analysis. AP wrote the initial draft of the manuscript through discussion with HK, FN, and EI. Idea of this study is proposed by HK. All authors have proofread the draft and approved the final manuscript.

Funding
A part of the donation from Hanshin Consultants for the endowed chair of "Sophisticated Earthquake Risk Evaluation", DPRI, Kyoto University was used.

Availability of data and materials
All data generated or analyzed during this study are included in this published article and referenced open sources of data.

Declarations

Ethics approval and consent to participate
Not applicable.

Consent for publication
Not applicable.

Competing interests
The authors declare that they have no competing interests.

Author details
[1]Geo-Research Institute, Otemae 2-1-2, Chuo-ku, Osaka 540-0008, Japan. [2]Disaster Prevention Research Institute, Kyoto University, Gokasho, Uji, Kyoto 611-0011, Japan.

Received: 2 June 2022 Accepted: 7 January 2023
Published online: 30 January 2023

References

Aoyagi Y, Kimura H, Mizoguchi K (2020) Seismic velocity structure at the southern termination of the 2016 Kumamoto Earthquake rupture, Japan. Earth Planets Space 72:142. https://doi.org/10.1186/s40623-020-01276-1
Asano K, Iwata T (2016) Source rupture processes of the foreshock and mainshock in the 2016 Kumamoto earthquake sequence estimated from the kinematic waveform inversion of strong motion data. Earth Planets Space 68:147. https://doi.org/10.1186/s40623-016-0519-9
Asano K, Iwata T (2021) Revisiting the source rupture process of the mainshock of the 2016 Kumamoto earthquake and implications for the generation of near-fault ground motions and forward-directivity pulse. Bull Seismol Soc Am 111:2426–2440. https://doi.org/10.1785/0120210047
Asano K, Sekiguchi H, Iwata T, Yoshimi M, Hayashida T, Saomoto H, Horikawa H (2016) Modelling of wave propagation and attenuation in the Osaka sedimentary basin, western Japan, during the 2013 Awaji Island earthquake. Geophys J Int 204:1678–1694. https://doi.org/10.1093/gji/ggv543
Bizzarri A (2012) Analytical representation of the fault slip velocity from spontaneous dynamic earthquake models. J Geophys Res 117:B06309. https://doi.org/10.1029/2011JB009097
Bouchon M, Toksoz MN, Karabulut H, Bouin MP, Dietrich M, Aktar M, Edie M (2002) Space and Time Evolution of Rupture and Faulting during the 1999 Izmit (Turkey) Earthquake. Bull Seismol Soc Am 92:256–266. https://doi.org/10.1785/0120000845
Eisner L, Clayton RW (2001) A reciprocity method for multiple-source simulations. Bull Seismol Soc Am 91:553–560. https://doi.org/10.1785/0120000222
Graves RW (1996) Simulating seismic wave propagation in 3D elastic media using staggered-grid finite differences. Bull Seismol Soc Am 86:1091–1106. https://doi.org/10.1785/BSSA0860041091

Graves R, Wald D (2001) Resolution analysis of finite fault source inversion using 1D and 3D Green's functions I. Strong Motions J Geophys Res 106:8767–8788
Graves R, Pitarka A (2004) Broadband time history simulation using a hybrid approach. Paper presented at the 13th World Conference on Earthquake Engineering, Vancouver BC, Canada, 1–6 August 2004. Paper 1098
Guatteri M, Mai PM, Beroza GC (2004) A pseudo-dynamic approximation to dynamic rupture models for strong ground motion prediction. Bull Seism Soc Am 94(6):2051–2063. https://doi.org/10.1785/0120040037
Hallo M, Gallovič F (2020) Bayesian self-adapting fault slip inversion with Green's functions uncertainty and application on the 2016 Mw7.1 Kumamoto earthquake. J Geophys Res 125:JB018703. https://doi.org/10.1029/2019JB018703
Hanks TC (1982) fmax. Bull Seism Soc Am 72:1867–1879. https://doi.org/10.1785/BSSA07206A1867
Hartzell SH, Heaton T (1983) Inversion of strong ground motion and teleseismic waveform data for the fault rupture history of the 1979 Imperial Valley, California, earthquake. Bull Seism Soc Am 73:1553–1583. https://doi.org/10.1785/BSSA07306A1553
Ikeda T, Kamae K, Miwa S, Irikura K (2002) Source characterization and strong ground motion simulation of the 2000 Tottori-ken Seibu earthquake using the empirical green's function method. J Struct Constr Eng AIJ 561:37–45
Inoue T, Miyatake T (1997) 3-D simulation of near-field strong ground motion: basin edge effect derived from rupture directivity. Geophys Res Lett 24:905–908. https://doi.org/10.1029/97GL00619
Irikura K (1986) Prediction of strong acceleration motions using empirical Green's function. In: Proceedings of the 7th Japan Earthquake Engineering Symposium, Tokyo, 1986, 151–156
Irikura K, Miyake H (2011) Recipe for predicting strong ground motion from crustal earthquake scenarios. Pure Appl Geophys 168:85. https://doi.org/10.1007/s00024-010-0150-9
Irikura K, Miyakoshi K, Kamae K, Yoshida K, Somei K, Kurahashi S, Miyake H (2017) Applicability of source scaling relations for crustal earthquakes to estimation of the ground motions of the 2016 Kumamoto earthquake. Earth Planets Space 69:10. https://doi.org/10.1186/s40623-016-0586-y
Irikura K, Kurahashi S, Matsumoto Y (2020) Extension of Characterized Source Model for Long-Period Ground Motions in Near-Fault Area. Pure Appl Geophys 177(5):2021–2047. https://doi.org/10.1007/s00024-019-02283-4
Iwata T, Sekiguchi H (2002) Rupture process and near-fault strong motions during the 2000 Tottori-ken Seibu earthquake. In: Proceedings of the 11th Japan Earthquake Engineering Symposium, Tokyo, 2002, 125–128
Kawase H, Matsushima S, Nagashima F, Baoyintu NK (2017) The cause of heavy damage concentration in downtown Mashiki inferred from observed data and field survey of the 2016 Kumamoto earthquake. Earth Planets Space 69:3. https://doi.org/10.1186/s40623-016-0591-1
Kobayashi G, Mamada Y, Wu C (2017) Analysis of the factors of large acceleration amplitude and estimation of the bedrock ground motions at the KiK-net Mashiki station caused by the maximum foreshock (M 627 j 6.5) of the 2016 Kumamoto earthquakes. J Japan Associ Earthquake Eng 17(4):101–139
Kobayashi H, Koketsu K, Miyake H (2017) Rupture processes of the 2016 Kumamoto earthquake sequence: causes for extreme ground motions. Geophys Res Lett 44:6002–6010. https://doi.org/10.1002/2017GL073857
Koketsu K, Miyake H, Suzuki H (2012) Japan Integrated Velocity Structure Model Version 1. Paper presented at the 15th World Conference on Earthquake Engineering, Lisbon, Portugal, 24–28 September 2012. Paper 1773
Kubo H, Suzuki W, Aoi S, Sekiguchi H (2016) Source rupture processes of the 2016 Kumamoto, Japan, earthquakes estimated from strong-motion waveforms. Earth Planets Space 68:161. https://doi.org/10.1186/s40623-016-0536-8
Kurita T (2017) Nonlinearity amplification of subsurface ground at KiK-net Mashiki site during the 2016 Kumamoto earthquake. J Japan Soc Civil Eng Struc Eng Earthquake Eng 73:74–82
Lagarias JC, Reeds JA, Wright MH, Wright PE (1998) Convergence properties of the nelder-mead simplex method in low dimensions. SIAM J Optim 9(1):112–147. https://doi.org/10.1137/S1052623496303470
Matsushima S, Kawase H (2000) Multiple asperity source model of the Hyogo-ken Nanbu earthquake of 1995 and strong motion simulation in Kobe. J Struct Constr Eng AIJ 534:33–40
Matsushima S, Kawase H (2009) Re-evaluation of strong motion and damage of wooden houses in Kobe city during the 1995 Kobe earthquake. J Struct Eng B 55B:537–543
Miyake H, Iwata T, Irikura K (2003) Source characterization for broadband ground-motion simulation: kinematic heterogeneous source model and strong motion generation area. Bull Seismol Soc Am 93:2531–2545. https://doi.org/10.1785/0120020183
Miyakoshi K, Petukhin A (2005) Delineation of the rupture velocity of heterogeneous source model extracted from source inversion results of inland earthquakes. Paper presented at the Joint Meeting of Earth and Planetary Science, Chiba, Japan, pp S046p-S52
Nakamura H, Miyatake T (2000) An approximate expression of slip velocity time functions for simulation of near-field strong ground motion. Zisin (J Seismol Soc Jpn) 53:1–9
Oglesby D, Mai PM (2012) Fault geometry, rupture dynamics and ground motion from potential earthquakes on the north Anatolian fault under the sea of Marmara. Geophys J Int 188:1071. https://doi.org/10.1111/j.1365-246X.2011.05289.x
Petukhin A, Iwasaki Y (2021) Validation of the Osaka basin model by reciprocal waveform simulation. Paper presented at the 6th IASPEI/IAEE International Symposium: Effects of Surface Geology on Seismic Motion, Kyoto, Japan, August 30–September 1, 2021. Paper GS5-P35
Petukhin A, Miyakoshi K, Tsurugi M, Kawase H, Kamae K (2016) Visualization of Green's function anomalies for megathrust source in Nankai trough by reciprocity method. Earth Planets Space 68:4. https://doi.org/10.1186/s40623-016-0385-5
Petukhin A, Sekiguchi H, Kawase H, Kamae K, Tsurugi M (2017) Large scale simulation of ground motions for heterogeneous source models by FDM reciprocity method. 24–28 Paper presented at the 16th World Conference on Earthquake Engineering, Santiago, Chile, 9–13 January 2017. Paper 2932
Petukhin A, Galvez P, Somerville P, Yoshida K, Miyakoshi K, Irikura K (2022) Multi-hypocenter rupture propagation validated from realistic multi-cycle earthquake simulation. Paper presented at the Japan Geoscience Union Meeting, Chiba, pp SSS10–SSS12
Pitarka A, Graves R, Irikura K, Miyakoshi K, Wu C, Kawase H, Rodgers A, McCallen D (2021) Refinements to the Graves-Pitarka Kinematic Rupture Generator, Including a Dynamically Consistent Slip-Rate Function, Applied to the 2019 Mw 7.1 Ridgecrest Earthquake. Bull Seismol Soc Am 112(1):287–306. https://doi.org/10.1785/0120210138
Poiata N, Miyake H, Koketsu K, Hikima K (2012) Strong-motion and teleseismic waveform inversions for the source process of the 2003 Bam, Iran. Earthquake Bull Seismol Soc Am 102(4):1477–1496. https://doi.org/10.1785/0120110198
Schmedes J, Archuleta RJ, Lavallée D (2010) Correlation of earthquake source parameters inferred from dynamic rupture simulations. J Geophys Res 115(B3):B03304. https://doi.org/10.1029/2009JB006689
Sekiguchi H, Aoi S, Honda R, Morikawa N, Kunugi T, Fujiwara H (2006) Rupture process of the 2005 West Off Fukuoka prefecture earthquake obtained from strong motion data of K-NET and KiK-net. Earth Planets Space 58:37–43. https://doi.org/10.1186/BF03351911
Sleep NH, Nakata N (2019) Nonlinear rheology at shallow depths with reference to the 2016 Kumamoto Earthquakes. Bull Seismol Soc Am 109(6):2674–2690. https://doi.org/10.1785/0120180200
Somei K, Miyakoshi K, Yoshida K, Kurahashi S, Irikura K (2019) Near-source strong pulses during two large *MJMA* 6.5 and *MJMA* 7.3 events in the 2016 2 Kumamoto, Japan, Earthquakes. Pure Appl Geophys 177:2223–2240. https://doi.org/10.1007/s00024-019-02095-6
The Headquarters for Earthquake Research Promotion (2017) Strong ground motion prediction method for earthquakes with specified source faults ("Recipe"). https://www.jishin.go.jp/main/chousa/17_yosokuchizu/recipe.pdf (in Japanese; last access April 2022)
The Headquarters for Earthquake Research Promotion (2019) Comprehensive active fault survey for the 2016 Kumamoto earthquake. Available via https://www.jishin.go.jp/main/chousakenkyuu/kumamoto_sogochousa/h28-h30/h28-h30kumamoto_sogochousa_3_3.pdf (in Japanese; last access October 2022).

Tinti E, Fukuyama E, Piatanesi A, Cocco M (2005) A kinematic source-time function compatible with earthquake dynamics. Bull Seismol Soc Am 95:1211–1223. https://doi.org/10.1785/0120040177

Tsurugi M, Kagawa T, Irikura K, Kowada A (1997) Basic research on the *fmax* value for earthquakes in Kinki region. Paper presented at the Japan Geoscience Union Meeting, Chiba

Tsurugi M, Tanaka R, Kagawa T, Irikura K (2020) High frequency spectral decay characteristics of seismic records of inland crustal earthquakes in Japan: evaluation of the *fmax* and κ models. Bull Seismol Soc Am 110:452–470. https://doi.org/10.1785/0120180342

Wu C, Koketsu K, Miyake H (2008) Source processes of the 1978 and 2005 Miyagi-oki, Japan, earthquakes: repeated rupture of asperities over successive large earthquakes. J Geophys Res 113:B08316. https://doi.org/10.1029/2007JB005189

Yoshida K, Hisada Y, Kawase H, Fushimi M (2005) Construction of vulnerability function of Japanese wooden houses for the best index of the destructive potential. In: Summaries of technical papers of Annual Meeting, Architectural Institute of Japan, Structures B- II:161-162

Yoshida K, Miyakoshi K, Somei K, Irikura K (2011) Source process of the 2011 off the Pacific coast of Tohoku Earthquake inferred from waveform inversion with long-period strong-motion records. Earth Planets Space 63:577–582. https://doi.org/10.5047/eps.2011.06.050

Yoshida K, Miyakoshi K, Somei K, Irikura K (2017) Source process of the Kumamoto earthquake (Mj 7.3) inferred from kinematic inversion of strong-motion records. Earth Planets Space 69:64. https://doi.org/10.1186/s40623-017-0649-8

Publisher's Note